



Fe vacancies in FeOCl enhanced reactive oxygen species generation for photocatalytic elimination of emerging pollutants

Zixuan Nie ^a, Chengji Sui ^a, Xiaobin Xie ^a, Shou-Qing Ni ^b, Lingshuai Kong ^b, Yifeng Wang ^a, Jinhua Zhan ^{a,b,*}

^a Key Laboratory of Colloid and Interface Chemistry, Ministry of Education, School of Chemistry and Chemical Engineering, Shandong University, Jinan 250100, China

^b Institute of Eco-Environmental Forensics, School of Environmental Science and Engineering, Shandong University, Qingdao 266237, China



ARTICLE INFO

Keywords:
Photocatalysis
O₂ activation
Fe vacancy
Organic pollutants
Reactive oxygen species

ABSTRACT

Reactive oxygen species (ROS) play an important role when using semiconductor photocatalysts in water remediation. Nonetheless, the insufficient conduction band potentials, as well as the limited mobility and quick recombination of charge carriers, often inhibit the ROS generation by many pristine photocatalysts. Here, we prepared FeOCl with tunable Fe-vacancy concentrations by using a NaCl-assisted thermal decomposition method. The defective FeOCl exhibited significantly higher rates of degradation and mineralization for organic pollutants compared to the non-defective FeOCl. This superior performance is attributed to the much faster superoxide (O₂^{·-}) and singlet oxygen (¹O₂) generation. Based on the experimental data and DFT simulations, Fe vacancies serve as electron trapping sites, leading to enhanced carrier lifetime and mobility, and can also reduce the conduction band potential of FeOCl, hence facilitating the formation of ROS. This study provides useful insights for developing cation-defected inorganic semiconductors and for improving the efficiency of O₂ activation in photocatalysis.

1. Introduction

Emerging organic pollutants, including endocrine disruptors, pharmaceutical and personal care products, and pesticides, have caused significant pollution in the aquatic environment worldwide [1–6]. This contamination has contributed substantially to the global water security issue to date [7,8]. The utilization of sunshine and molecular oxygen (O₂) by photocatalytic processes has long been considered an ideal approach for the elimination of POPs in wastewater [9,10]. When O₂ is activated by photocatalysts under sunlight irradiation, the reactive oxygen species (ROS) produced are capable of breaking down and even completely mineralizing most emerging pollutants [11]. Iron oxychloride (FeOCl) has recently been exploited as a potent photocatalyst for O₂ activation, owing to its narrow band gap energy (ca. 1.8 eV), tunable electronic characteristics, and minimal photocorrosion [12–14]. Nonetheless, these advantages are far from ideal for efficient photocatalytic water remediation applications [15]. Due to the quick electron-hole pair recombination, the carrier concentration on FeOCl surfaces is low [16]. Moreover, the dominating carriers in n-type FeOCl,

namely, the photogenerated electrons, have relatively low reducing activity. These factors cause FeOCl's activation of O₂ to generate ROS to be inefficient [17,18]. It remains highly desirable to improve the performance of FeOCl in photocatalytic O₂ activation for generation of ROS in order to further develop its application in water remediation.

Recently, multiple studies have documented the improvement in the effectiveness of ROS production in the FeOCl photocatalytic systems. The methods used mostly revolve around the construction of heterojunction composite systems [13,16,19–22]. Nevertheless, the efforts to improve the intrinsic photocatalytic capabilities of FeOCl are currently very scarce. Enhancing the intrinsic performance of photocatalysts is more conducive to realizing their full application potential. For other photocatalysts like TiO₂ and C₃N₄, multiple studies have shown that surface defects play a crucial role in controlling the spin nature, carrier concentration, and energy band structure, so that they can alter the inherent properties of photocatalytic materials and thereby increase the photocatalytic activity [23–27]. Therefore, we anticipate that defect engineering could be an useful approach to improve the inherent photocatalytic properties of FeOCl and enhance its performance in

* Corresponding author at: Key Laboratory of Colloid and Interface Chemistry, Ministry of Education, School of Chemistry and Chemical Engineering, Shandong University, Jinan 250100, China.

E-mail address: jhzhan@sdu.edu.cn (J. Zhan).

photocatalytic O_2 activation [28]. Among the various types of defects, cationic vacancies are a classic type of defect that plays a crucial role in photocatalytic processes [29]. Cationic vacancies can modulate the energy band structure by shifting the VB maxima upward and the CB minima downward without creating new intermediate states [30]. In addition, cationic vacancies are able to act as the transfer channels for carrier migration, thereby accelerating the charge carrier transfer and promoting the separation efficiency of photo-generated carriers [30,31]. The modulation of energy bands and electronic structures induced by cationic vacancies will be promising to improve the performance of FeOCl photocatalytic activation of O_2 . However, it is less explored relative to anionic defects such as O vacancies, due to the lack of facile approaches for preparing of cation-defected semiconductors and modulating of the concentration of the vacancies. This may be caused by the large formation energy [32]. To our knowledge, FeOCl with Fe vacancies has not been investigated. Further investigation is also required to understand the mechanism of the role of Fe vacancies in the photocatalytic activation of the O_2 reaction.

Herein, we have successfully realized the preparation of FeOCl with controllable Fe vacancy concentration using a facile method of NaCl-assisted thermal decomposition. Fe vacancies improved the charge separation and transport efficiency of FeOCl, and modulated the energy band structure of FeOCl, which facilitate the activation of O_2 to generate ROS, such as O_2^\bullet and 1O_2 . Benefit from the high ROS generation rate, FeOCl exhibited significantly higher rates of degradation (14 times higher) and mineralization for organic pollutants compared to the non-defective FeOCl. The degradation kinetics, pollutant scope, influence of coexisting ions and humic acid, and the effects of various water bodies were evaluated. Our results indicate that the Fe-defected FeOCl is promising in real water treatment processes. The microscopic structure, electronic structure, interfacial charge transfer, photogenerated charge carriers, and photo-response, were systematically studied by experimental techniques and DFT simulation. We found Fe vacancies serve as electron trapping sites, leading to enhanced carrier lifetime and mobility, and can also reduce the conduction band potential of FeOCl, hence facilitating the formation of ROS. Our findings provide useful insights for developing cation-defected inorganic semiconductors and for improving the efficiency of O_2 activation in photocatalysis.

2. Materials and methods

Supporting Information Text S1 provides a comprehensive description of chemicals, characterization instruments, and analytical methods.

2.1. Preparation procedures

The FeOCl sample with rich Fe vacancies were synthesized by a thermal decomposition method [33]. 5.0 g of $FeCl_3 \cdot 6H_2O$ and 0.15 g of NaCl were dissolved in 5 mL of deionized water in a glass beaker. The beaker was then heated in an oven at 70 °C for 15 h to remove most of the moisture from it. The above beaker was put in a pit furnace and heated at 240 °C for 90 min. The atmosphere was air and the rate of heating was 10 °C/min. After cooling to room temperature, the samples were crushed and rinsed with plenty of deionized water and acetone. The washed samples were dried at 60 °C overnight. FeOCl with rich Fe vacancies was collected after drying, named $V_{Fe}\text{-FeOCl}$.

The concentration of Fe vacancies in FeOCl can be controlled by adjusting the dosage of NaCl. The amount of NaCl was reduced to 0.03 g to prepare FeOCl with less Fe vacancies. This sample was used as a reference material, named $V_{Fe}\text{Poor-FeOCl}$ ($V_{Fe}\text{P-FeOCl}$). Accordingly, pure FeOCl was obtained by the same preparation method without the addition of NaCl.

2.2. Photocatalytic degradation experiments

Bisphenol A (BPA) as a model pollutant was used to evaluate the

catalytic potency of the prepared samples for degradation of BPA (10 mg/L) under simulated AM-1.5 (1 SUN, 1000 W·m⁻²) solar irradiation. A xenon lamp (LSH-X500) was used as a simulated sunlight source, and the irradiated area was 6 cm². In a typical experiment of photocatalysis, 5 mg photocatalyst was added to 9 mL deionized water in a glass tube (outer diameter = 20 mm; volume = 50 mL). After ultrasonication of 3 min for dispersion, 1 mL of 100 ppm BPA solution was added into the above glass tube. Then, air was bubbled in the dark for 30 min to achieve adsorption and desorption equilibrium. At the specific time, 1 mL of reaction solution was taken and immediately quenched with ethanol, and the suspension was filtered through a 0.22 μm membrane filter for analysis. A similar experimental procedure was utilized to determine the degradation efficiency of the other pollutants such as 4-chlorophenol, nitrobenzene, chloramphenicol and acetaminophen.

2.3. Theoretical calculations

The Vienna ab initio simulation package (VASP) 6.1.0 was used to carry out all the DFT calculations [34]. The spin-polarized generalized gradient approximation (GGA) technique with the Perdew–Burke–Ernzerhof (PBE) functional with D3 dispersion correction was employed. [35,36]. The utilization of the projector augmented wave (PAW) method allowed for the depiction of the fundamental operations of the atoms, with the energy of the wavefunctions determined at 500 eV. The wavefunctions were in a state of complete relaxation until there was a shift in electronic energy and the alteration in eigenvalues was less than 10⁻⁵ eV. The structures were fully relaxed until the maximal force on each atom was less than 0.02 eV/Å. $V_{Fe}\text{-FeOCl}$ was built from 3 × 3 × 1 FeOCl supercell. The 4 × 4 × 2 and 1 × 1 × 2 Monkhorst-Pack grids were used for FeOCl and $V_{Fe}\text{-FeOCl}$, respectively. The electronic levels were occupation by setting Gaussian smearing with a width of σ = 0.1 eV. The rotationally invariant DFT+U was employed to describe the local Coulomb interactions between 3d electrons. The values of U of 5.3 eV are used for Fe-3d orbitals.

3. Results and discussion

3.1. Structural characterizations

Fig. 1a depicts the NaCl-assisted thermal decomposition procedure for the preparation of FeOCl with Fe vacancies. It has been reported that during the thermal decomposition of $FeCl_3 \cdot 6H_2O$, Cl tend to be stripped as HCl and HClO, O tend to be stripped synchronously as HClO, leading to pure FeOCl with 1:1:1 at. ratio [37]. The addition of NaCl was found to be effective in controlling the atomic proportion of Fe, O, and Cl, promoting the formation of FeOCl with Fe vacancies. This is confirmed findings of thermogravimetric mass spectrometry (TG-MS) analysis (**Fig. S1**). The release of HClO decreases significantly, suggesting that the decomposition process retains more O. The addition of NaCl provided sufficient additional Cl. Consequently, excess Cl and O leads to the inadequate supply of Fe and formation of Fe vacancies in FeOCl [38,39]. To confirm the role of NaCl, we prepared two samples possessing different Fe vacancies concentrations, FeOCl with Fe vacancies ($V_{Fe}\text{-FeOCl}$) and FeOCl with less Fe vacancies ($V_{Fe}\text{P-FeOCl}$) by controlling the amount of NaCl added. The loadings of Fe vacancies increase from FeOCl to $V_{Fe}\text{P-FeOCl}$, and then to $V_{Fe}\text{-FeOCl}$ as more and more NaCl was used.

X-ray diffraction (XRD) and Raman spectrum was used to analyze the phases of $V_{Fe}\text{-FeOCl}$, $V_{Fe}\text{P-FeOCl}$ and FeOCl. **Fig. 1b** shows all the XRD peaks of $V_{Fe}\text{-FeOCl}$ are well indexed to the standard card of FeOCl (JCPDS no. 72-0619). According to the analysis of peak width at half maxima, the $V_{Fe}\text{-FeOCl}$ material exhibits a little lower level of crystallinity compared to FeOCl (**Table S1**). In addition, there is no apparent shift in the peak position of the (010) facet in $V_{Fe}\text{P-FeOCl}$ and $V_{Fe}\text{-FeOCl}$, providing preliminary evidence that no Na^+ was inserted into the FeOCl interlayer (**Fig. S2**) [40]. The non-detection of Na^+ in $V_{Fe}\text{P-FeOCl}$ and $V_{Fe}\text{-FeOCl}$ by ICP-MS further confirms this. As shown in **Fig. S3a**, the

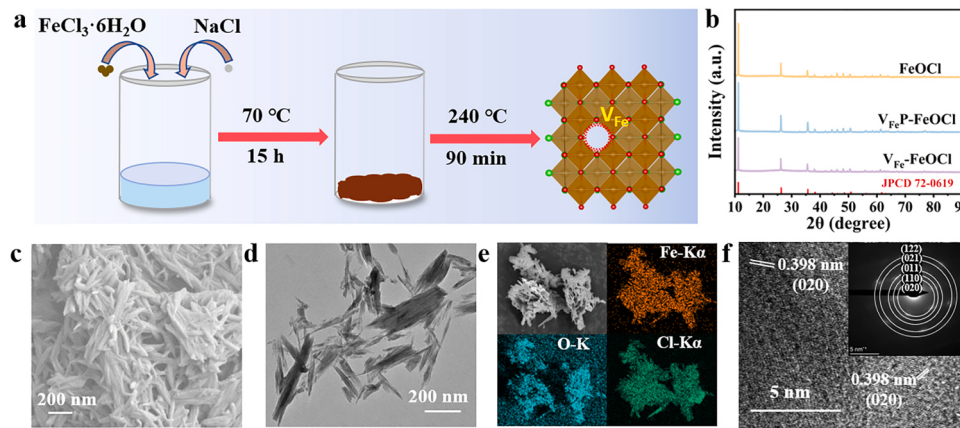


Fig. 1. (a) Schematic illustration for the synthesis of V_{Fe}-FeOCl. (b) XRD patterns of FeOCl, V_{Fe}P-FeOCl, and V_{Fe}-FeOCl. (c) SEM image of V_{Fe}-FeOCl. (d) TEM image of V_{Fe}-FeOCl. (e) HAADF-STEM and corresponding EDS mapping images of V_{Fe}-FeOCl. (f) HRTEM image (inset shows the SAED pattern).

Raman spectrum of pure FeOCl shows a peak at 214 cm⁻¹ attributed to the Fe-Cl stretching mode, and the peaks at 280 and 394 cm⁻¹ are attributed to the Fe-O stretching mode [41]. Significant negative shifts and broadening are observed in the Raman peaks of V_{Fe}P-FeOCl and V_{Fe}-FeOCl, in comparison to FeOCl. The alteration in the long-range arrangements of the crystals may be the cause, consistent with the more Fe-defects in V_{Fe}P-FeOCl and V_{Fe}-FeOCl [42]. In the microstructures by SEM and TEM, pure FeOCl shows the typical laminated morphology (Fig. S4a and b). The added NaCl induces the formation of needle-like particles with smaller size (Fig. S4c and d). Ultimately, all the particles of V_{Fe}-FeOCl show the spindle-like shape with lengths ranging 0.2–1.0 μm agglomerated by needle-like particles (Fig. 1c and d). The EDS mapping profiles on V_{Fe}-FeOCl exhibit a uniform distribution of the elements Fe, O, and Cl (Fig. 1e). Furthermore, the SAED pattern confirms the crystal structure of V_{Fe}-FeOCl (Fig. 1f). There, the lattice spacings of V_{Fe}-FeOCl are consistent with the (020) and (110) planes of FeOCl [43,44]. The BET surface area of FeOCl and V_{Fe}-FeOCl was calculated using N₂ absorption-desorption isotherm (Fig. S5). All the samples exhibit type IV isotherm [37]. V_{Fe}-FeOCl (22.1 m²·g⁻¹) has a larger BET area than FeOCl (7.3 m²·g⁻¹).

Additional comprehensive characterizations were performed to further characterize the Fe-vacancies. In the electron paramagnetic resonance (EPR) spectra, V_{Fe}P-FeOCl and V_{Fe}-FeOCl display a similar signal at approximately $g = 2.002$ (Fig. 2a), which can be attributed to the electrons trapped in the iron vacancies [42,45]. V_{Fe}-FeOCl has the highest signal intensity, indicating the highest loading of vacancies. The atomic contents of the samples were analyzed using inductively coupled plasma mass spectrometry (ICP-MS) and ion chromatography (IC). As the concentration of vacancies increases, the Fe contents in samples decrease significantly, and the Cl and O contents increase at the same time, suggesting that the predominant defect type is Fe vacancies (Fig. 2b and Table S2). And further using the variation of atomic ratios, the content of Fe vacancies in V_{Fe}P-FeOCl and V_{Fe}-FeOCl is estimated as 2.1% and 7.2% [42,46,47]. X-ray absorption fine structure spectroscopy (XAFS) was employed to analyze the coordination structures of Fe atoms in V_{Fe}-FeOCl and FeOCl at an atomic level. The k-edge shifts in the direction of higher binding energy from FeOCl to V_{Fe}-FeOCl, indicating that the valence state of Fe increases (Fig. 2c) [48]. This coincides with the observations by using X-ray photoelectron spectroscopy (XPS; Fig. S3b and c). In the XPS spectra, a slight rise in binding energy is observed when comparing FeOCl to V_{Fe}-FeOCl, which corresponds to an increase of the average Fe valence from 2.50 to 2.64. Both the results of the XAFS and XPS spectra are consistent with the existence of cationic vacancies [49,50]. The R-space curve allows us to determine the information of the ligand atoms. The positions of the peaks indicate the bond lengths of the ligand atoms, and the intensities reflect the disorder of the

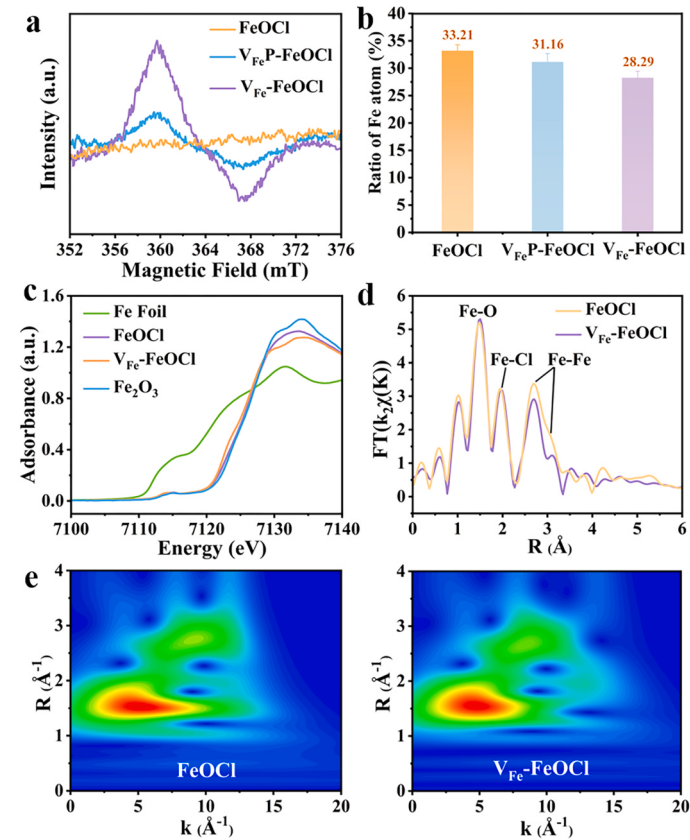


Fig. 2. (a) EPR spectra of FeOCl, V_{Fe}P-FeOCl, and V_{Fe}-FeOCl. (b) Fe atom ratios in FeOCl, V_{Fe}P-FeOCl, and V_{Fe}-FeOCl. (c) Fe K-edge XANES spectra of FeOCl, V_{Fe}-FeOCl, and Fe foil and Fe₂O₃. (d) The Fe K-edge Fourier-transformed EXAFS spectra of FeOCl and V_{Fe}-FeOCl. (e) WT-EXAFS plots of FeOCl and V_{Fe}-FeOCl.

internal structure of the samples and the number of coordinating atoms. The Fe-O and Fe-Cl peaks marked in the spectrum of V_{Fe}-FeOCl have similar intensity to those of FeOCl, while the Fe-Fe peak intensity is smaller due to the existence of Fe vacancies (Fig. 2d) [51]. We summarize the Fe coordination numbers obtained by fitting the spectra with EXAFS curve-fitting routines (Fig. S6). The formation of Fe vacancies in V_{Fe}-FeOCl can also be reflected by a smaller coordination number (CN) of the Fe-Fe shells in Table S3 (CN_{Fe-Fe} = 3.6 and 1.7 for V_{Fe}-FeOCl vs. CN_{Fe-Fe} = 4 and 2 for FeOCl), because of the absence of Fe atoms at the defect sites [52]. No O or Cl vacancies exist in V_{Fe}-FeOCl, because its CNs

of Fe-O shells and Fe-Cl shells are essentially the same as those of FeOCl, which are close to the theoretical value of 6 for the octahedral structure [43]. In line with the above results, the WT-EXAFS plots of FeOCl and V_{Fe}-FeOCl also confirm the exclusive existence of Fe-Fe and Fe-O coordination (Fig. 2e). To summarize, we successfully fabricated the V_{Fe}-FeOCl material rich in Fe vacancies by using a NaCl-assisted pyrolysis approach. This method also enables us to regulate the vacancy concentration.

3.2. The photocatalytic degradation performance

The photocatalytic degradation performances of V_{Fe}-FeOCl for organic pollutants in wastewater were investigated using BPA as the model persistent organic pollutant. The control studies indicate that adsorption is minimal, and the degradation process necessitates the presence of photocatalysts, light irradiation, and O₂ (Fig. 3a). Within 25 min, V_{Fe}-FeOCl degraded 100% of BPA, while pure FeOCl only degraded 20.9%. Moreover, V_{Fe}-FeOCl was more efficient than V_{Fe}P-FeOCl, indicating the degradation efficiency of BPA increases with the loading of Fe-vacancy. The degradation kinetics could be modeled using the pseudo-first-order kinetic equation (Fig. S7) [53]. V_{Fe}-FeOCl has the largest rate constant (0.168 min⁻¹), which is 14 times that of FeOCl (0.012 min⁻¹, Fig. 3b). By comparing the BPA degradation rate and first-order rate constants, V_{Fe}-FeOCl is outstanding compared to state-of-the-art photocatalysts (Table S4). We also investigated the potential of V_{Fe}-FeOCl to degrade BPA when exposed to real sunlight. To our delight, it has remarkable photocatalytic efficiency, with about 99.8% of BPA degraded in 100 min (Fig. S8). We detected the iron dissolution from the V_{Fe}-FeOCl system during the photocatalytic process and further investigated the effect of dissolved iron on BPA degradation (Fig. S9). The contribution of the homogenization reaction can be excluded due to the negligible degradation of BPA by dissolved iron.

According to HPLC-MS analyses, the degradation intermediates of BPA of the V_{Fe}-FeOCl system includes phenol, p-isopropenyl phenol, hydroquinone, 1-(3,4-dihydroxyphenyl)ethan-1-one, benzoquinone, 2-hydroxyacetic acid, and 2-hydroxypropionic acid (Table S5 and Fig. S10). The degradation pathways of BPA, dominated by ¹O₂ and O₂^{•-}, are presented below. In the first step, the β -scission of isopropyl between two phenyl groups in BPA leads to the degradation of BPA, which is triggered by ROS (¹O₂ and O₂^{•-}) and the production of phenol and p-isopropenyl phenol [54]. In the second step, the formed phenol and

p-isopropenyl phenol are further hydroxylated by ¹O₂ to 1-(3,4-dihydroxyphenyl)ethan-1-one and finally to p-benzoquinone, which is easily decomposed [55]. In parallel to that, the previously formed aromatic intermediates are further decomposed to simple organic acids (2-hydroxyacetic acid, and 2-hydroxypropionic acid) by ring-opening reaction and then mineralized to CO₂ and H₂O by combined oxidation of ¹O₂ and O₂^{•-}. It is worth noting that all of these compounds are biodegradable [56].

Fig. 3c shows the temporal changes in the total organic carbon (TOC). After 20 min, when 97% of BPA had been degraded, the V_{Fe}-FeOCl system achieved a 38.2% reduction in TOC. The elimination of TOC increased steadily and ultimately reached a level of 62.8%. In contrast, by the FeOCl system, TOC removal was only 7.4% within 20 min, while hardly increased with prolonging the reaction time. Therefore, V_{Fe}-FeOCl not only degrades BPA in a higher rate, but also in a higher mineralization efficiency. Based on the successful application of V_{Fe}-FeOCl in the photocatalytic degradation and mineralization of BPA, the degradation of other organic pollutants was also examined. All the organic pollutants, including phenol (BP), 4-chlorophenol (4-CP), nitrobenzene (NBz), acetaminophen (APAP) and chloramphenicol (CAP), were completely photocatalytically degraded by V_{Fe}-FeOCl within a short reaction period (Fig. 3d). Reusability of photocatalysts is crucial in wastewater treatment. To investigate the reusability of V_{Fe}-FeOCl, we performed five consecutive cycles of BPA degradation experiments (Fig. 3e). The activity of V_{Fe}-FeOCl remained essentially unchanged. Meanwhile, SEM and XRD were used to characterize the morphology and structure of the recycled V_{Fe}-FeOCl after five runs. Fig. S11 shows that the structure and morphology of the catalysts maintained a high degree of consistency after five cycles of recycling, verifying the stability of V_{Fe}-FeOCl in water remediation.

During the wastewater treatment processes of organic pollutants, the photocatalytic activity of a photocatalyst can be affected by the pH of the wastewater, coexisting ions, dissolved organic matter, and other environmental factors. As shown in Fig. 3f, the acidic environment facilitated the degradation of BPA, while the alkaline environment slightly hindered its degradation. This is because the higher the acidity of the solution (pH < 4.8), the more positive the redox potential of O₂/O₂^{•-} is, which is more favorable for the conversion of O₂ to ROS [18]. Increasing the concentrations of ROS promotes the degradation of BPA. In the alkaline environments, excess OH⁻ induces charge repulsion thereby interfering with the participation of photogenerated electrons in

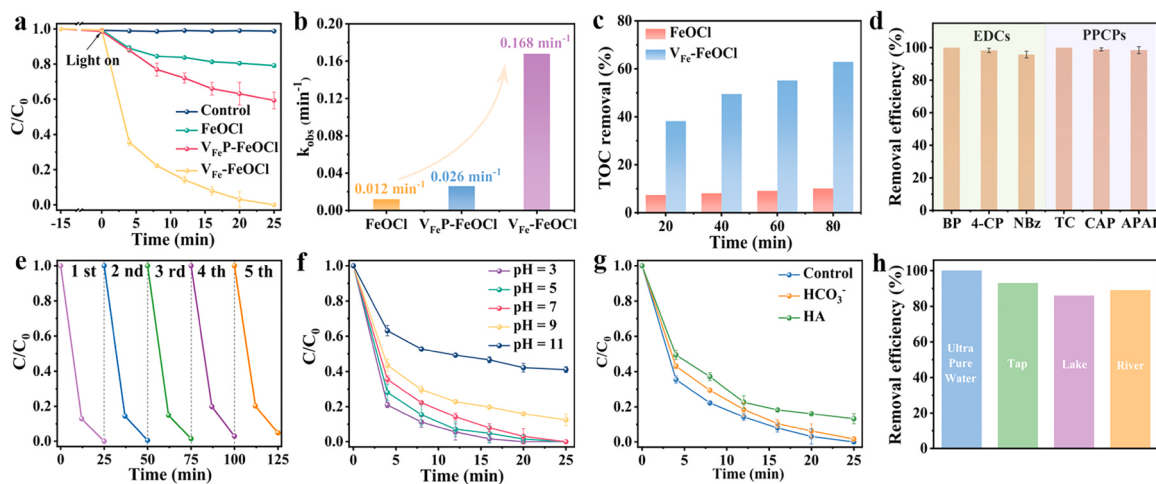


Fig. 3. (a) The degradation kinetics by the various systems under simulated solar light irradiation. Catalyst loading = 0.5 g/L and [BPA]₀ = 10 mg/L. The -15–0 min range shows the adsorption is negligible. (b) The first-order rate constants for FeOCl, V_{Fe}P-FeOCl, and V_{Fe}-FeOCl. (c) TOC removal by FeOCl and V_{Fe}-FeOCl. (d) The degradation of six organic pollutants (44 μ M) by V_{Fe}-FeOCl, including phenol (BP), 4-chlorophenol (4-CP), nitrobenzene (NBz), tetracycline (TC), chloramphenicol (CAP), and acetaminophen (APAP). (e) BPA degradation efficiency by V_{Fe}-FeOCl in five consecutive cycles. Effects of (f) pH, (g) HCO₃⁻ and HA on photocatalytic degradation of BPA (10 mg/L) by V_{Fe}-FeOCl. (h) The degradation efficiency of BPA by V_{Fe}-FeOCl photocatalysis within 30 min in different water bodies.

O_2 activation [57]. Nonetheless, V_{Fe} -FeOCl exhibited high degradation efficiency over a wide pH working window. Humic acid (HA) and HCO_3^- were used to explore the tolerance of V_{Fe} -FeOCl to dissolved organic matter and coexisting ions. Fig. 3g shows that HA and HCO_3^- , even at high concentrations (5.0 mM), had negligible inhibitory effect on the BPA degradation. Therefore, the V_{Fe} -FeOCl photocatalyst exhibited high selectivity to the organic pollutants. Furthermore, the performance of V_{Fe} -FeOCl was also excellent in a variety of water sources (Fig. 3h). Overall, the performance of V_{Fe} -FeOCl was largely unaffected by various factors present in real water environments, indicating significant potential for use in wastewater treatment.

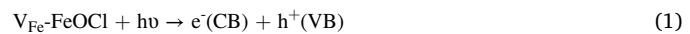
3.3. Efficient ROS generation

To investigate the ROS produced by the V_{Fe} -FeOCl photocatalyst, DMPO and TEMP were used as spin-trapping agents during the EPR tests. As shown in Fig. 4a, the sextet signals when using DMPO indicates that O_2^- was produced, whereas in Fig. 4c, the triplet signals with 1:1:1 peak height when using TEMP indicates the formation of 1O_2 . Therefore, V_{Fe} -FeOCl generated both O_2^- and 1O_2 during the photocatalytic degradation of the organic pollutants. The signal strength of both O_2^- and 1O_2 in the V_{Fe} -FeOCl system is considerably higher than that of FeOCl. In addition, hydroxyl radicals ($\bullet OH$) were also examined, and the absence of the characteristic quadrupole peaks of $\bullet OH$ (intensity ratio of 1:2:2:1) confirmed the absence of $\bullet OH$ radical generation (Fig. S13). The precise quantity of the ROS produced was determined, as shown in Fig. 4b. The concentrations of 1O_2 and O_2^- in the V_{Fe} -FeOCl system reached 0.38 and 0.55 mM, respectively, within 30 min. These concentrations are 11.5 and 275 times greater than those detected in the FeOCl system, which are 0.033 and 0.002 mM, respectively. The enhanced production of the ROS by V_{Fe} -FeOCl demonstrates that the introduction of Fe vacancies enhances the photocatalytic activation of O_2 into ROS.

To further ascertain the roles of the ROS in the V_{Fe} -FeOCl photocatalytic system, we carried out the quenching experiments. As shown in Fig. 4d, tempol (O_2^- scavenger) and FFA (1O_2 scavenger) inhibited the degradation of BPA, leading to only 37.7% and 42.2% of BPA degradation after 25 min, respectively. Hence, O_2^- and 1O_2 are the major

reactive species responsible for the photocatalytic degradation of BPA. $K_2Cr_2O_7$ (electron scavenger) also substantially inhibited the degradation, due to cutting off the pathway of O_2 in formation of O_2^- , further suggesting the important roles of O_2^- and 1O_2 in the degradation [14,57, 58]. EDTA-2Na (hole scavenger) also inhibited the degradation of BPA to a certain extent, suggesting that holes are also involved in the degradation of BPA or ROS generation. In contrast, TBA and catalase did not induce inhibition of BPA degradation. Hence, $\bullet OH$ radicals, and H_2O_2 are not responsible for the degradation reaction. In all, the higher efficiency of V_{Fe} -FeOCl than FeOCl must be attributed to the more generation of ROS by the V_{Fe} -FeOCl system. Combined with quenching experiments and BPA degradation experiments in real water samples, the generation of 1O_2 improves the degradation and mineralization rate of the system. Additionally, it enhances the anti-interference ability of the V_{Fe} -FeOCl/ O_2 system, greatly increasing its potential for practical applications [59].

We also examined the origin of O_2^- and 1O_2 (Fig. S14). The degradation of BPA was significantly inhibited when the dissolved oxygen concentration was reduced using N_2 . Correspondingly, the degradation efficiency of BPA by V_{Fe} -FeOCl was improved with the increase of dissolved O_2 concentration by bubbling O_2 . These phenomena demonstrate that oxygen concentration is a major factor in the degradation of organic pollutants and V_{Fe} -FeOCl can effectively photoactivate oxygen to produce ROS for the degradation process [57]. Based on the above results, we can propose the process of O_2 activation to generate the ROS in this system. First, V_{Fe} -FeOCl generates electrons (e^-) and holes (h^+) under light irradiation (Eq. 1). The photo-generated electrons react with the O_2 molecules near the photocatalyst surfaces, resulting in the formation of O_2^- (Eq. 2) [15]. 1O_2 is formed through two routes: accepting energy from excited photocatalyst (Eq. 3) and oxidation of O_2^- by h^+ (Eq. 4) [11]. This can be demonstrated by ESR quenching experiments, which showed that both EDTA-2Na and Cr(VI) significantly inhibit the generation of 1O_2 and the inhibition effect of Cr(VI) is more obvious (Fig. S15).



3.4. Structural roles for efficient ROS generation

The structure-activity relationship on the efficient generation of ROS by the Fe-defected FeOCl were studied. The UV-vis diffuse reflectance spectra (DRS) were utilized to analyze the photo-absorption properties. The DRS spectra in Fig. 5a demonstrate that Fe vacancies boost the photo-absorption of FeOCl. The absorption edge of V_{Fe} -FeOCl shows a considerable red-shift in comparison to FeOCl, which can be attributed to the presence of Fe vacancies [60]. The bandgap energies of FeOCl, $V_{Fe}P$ -FeOCl, and V_{Fe} -FeOCl are approximated to be 1.81, 1.73 and 1.67 eV, respectively (Fig. 5b). The valence band (VB) potentials of the samples were determined by the XPS VB spectra. The VB potentials are 1.76, 1.50, and 1.33 eV vs. NHE for FeOCl, $V_{Fe}P$ -FeOCl, and V_{Fe} -FeOCl, respectively (Fig. 5c). The conduction band (CB) potentials for FeOCl, $V_{Fe}P$ -FeOCl, and V_{Fe} -FeOCl (Fig. 5d) are determined by these values and the bandgap values, which are -0.05 , -0.23 , and -0.34 eV (vs. NHE), respectively. It can be seen that the introduction of Fe vacancies exerts a substantial effect on the electronic structure of FeOCl. As a result, E_{CB} of V_{Fe} -FeOCl (-0.34 eV) becomes more negative compared to $E(O_2/O_2^-)$ which is -0.33 V, thus facilitating the formation of O_2^- and the further oxidation of O_2^- to 1O_2 [18]. The effect of iron vacancies on the energy band of FeOCl was further explored using DFT calculations (Fig. 5e and

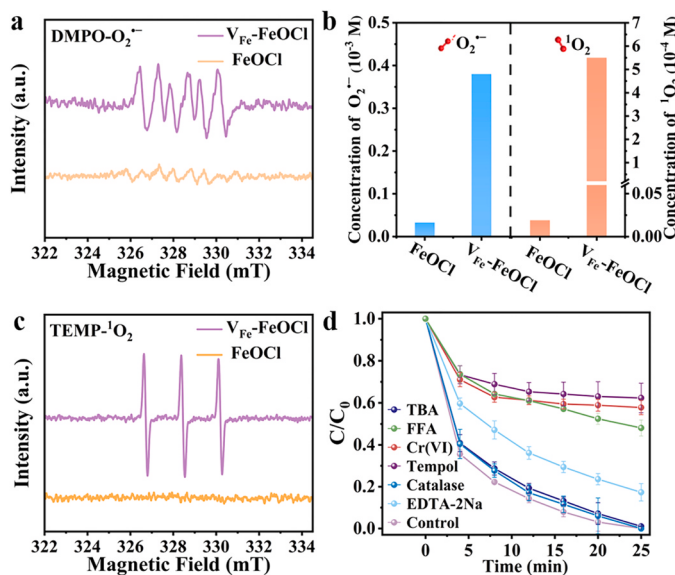


Fig. 4. ESR spectra of DMPO-trapped O_2^- (a) and TEMP-trapped 1O_2 (c). (b) The produced amount of O_2^- and 1O_2 during 30 min of photocatalytic reaction. (d) The effects of the scavengers in the photocatalytic degradation of BPA (10 mg/L) by V_{Fe} -FeOCl (0.5 g/L). The added concentrations are: 2 mM tertiary butanol (TBA), 200 units/mL catalase, 2 mM Tempol, 2 mM EDTA-2Na, 10 mM furfuralcohol (FFA), 1 mM $K_2Cr_2O_7$.

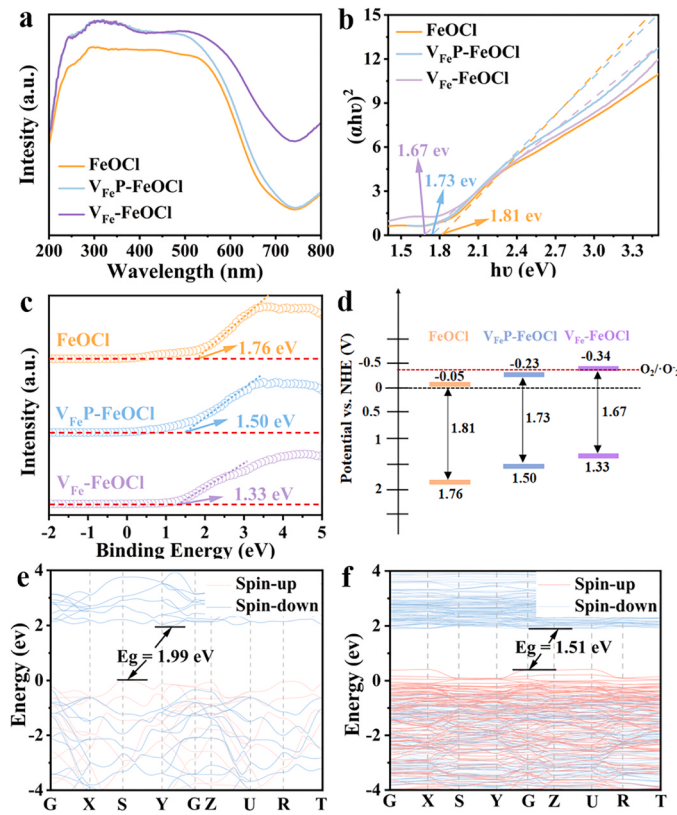


Fig. 5. (a) UV-vis diffuse reflectance spectra and (b) band-gap energy of different photocatalysts. (c) VB XPS spectra and (d) bandgap energies diagram of different photocatalysts. Calculated energy band structures of FeOCl (e) and V_{Fe}-FeOCl (f).

f). The calculated band gap of V_{Fe}-FeOCl (1.51 eV) is much smaller than that of FeOCl (1.99 eV), consistent with the experimental results.

Electrochemical impedance spectroscopy (EIS) was employed to investigate carrier transfer and interfacial reaction efficiency of the photocatalysts (Fig. 6a). For the samples with higher Fe-vacancy concentrations, the arc radii of the spectra are larger. The smaller arc radius of V_{Fe}-FeOCl reflects a lower resistance of charge transfer at the V_{Fe}-FeOCl/solvent interface in comparison to FeOCl, which is favorable enhancement of the charge transfer routes promoting generation of O₂[·] and ¹O₂ [24,45]. Benefiting from these advantages, V_{Fe}-FeOCl generated notably stronger photocurrent than FeOCl and V_{Fe}P-FeOCl (Fig. 6b) [49]. The charge carrier density of a photocatalyst can be calculated by the slope of its Mott-Schottky curve (Fig. 6c). V_{Fe}-FeOCl has a higher charge carrier density than V_{Fe}P-FeOCl, followed by FeOCl. Obviously, the high charge carrier density in V_{Fe}-FeOCl benefits the interfacial charge transfer and energy transfer to generate O₂[·] and ¹O₂. [61]. The charge-separation efficiency and the lifetime of photogenerated charge carriers of the photocatalysts were assessed through photoluminescence (PL) and time-resolved PL spectra (Fig. 6d and Fig. S16). The spectra show a charge recombination signal at about 623 nm. As the concentration of Fe vacancies increases from FeOCl to V_{Fe}P-FeOCl and to V_{Fe}-FeOCl, the PL intensity decreases sharply, indicating that V_{Fe}-FeOCl has the most substantial carrier separation and transport efficiency. This conclusion is similarly confirmed by the time-resolved PL spectra, which shows the PL average lifetime follows the order FeOCl < V_{Fe}P-FeOCl < V_{Fe}-FeOCl. The better charge separation and longer lifetime of V_{Fe}-FeOCl are mainly due to the Fe vacancies that serve as separation centers, capturing more photo-generated electrons to promote the conversion of O₂ to ROS [23,62]. The density of states (DOS) functions of FeOCl and V_{Fe}-FeOCl were calculated (Fig. 6e and f). Compared to pure FeOCl, the introduction of iron vacancies leads to significant

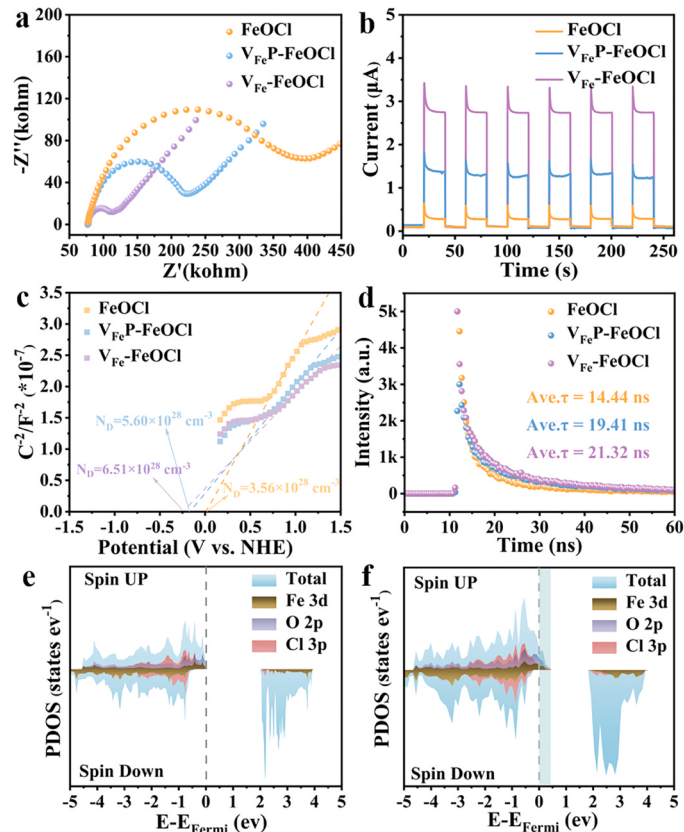


Fig. 6. (a) The electrochemical impedance spectra and (b) photocurrent response of different photocatalysts. (c) Mott-Schottky plots of different photocatalysts. (d) The nanosecond-level fluorescence decay spectra of different photocatalysts. Partial density of states (PDOS) spectra of FeOCl (e) and V_{Fe}-FeOCl (f).

electronic delocalization of neighboring atoms, resulting in a significant increase in the density of states of the spin-up component above the Fermi level, exhibiting typical half-metallicity characteristics [52,63]. This leads to a significant improvement in the conductivity of V_{Fe}-FeOCl compared to FeOCl, which boosts carrier mobility and enhances the O₂ activation process [64]. The calculated results are in excellent agreement with the electrochemical impedance spectra and photocurrent measurements.

Taken together, the boosted formation of O₂[·] and ¹O₂ is responsible for the enhanced photocatalytic degradation and mineralization of the persistent organic pollutants by the Fe-vacancy containing photocatalysts, specifically, V_{Fe}-FeOCl. The enhanced generation of O₂[·] and ¹O₂ is attributable to three main factors: the modulated energy band, enhanced charge separation, and accelerated dynamics of interfacial

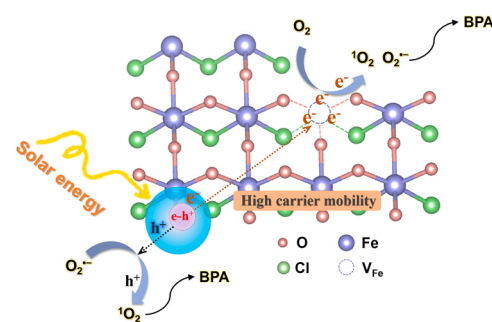


Fig. 7. Mechanism of Fe vacancy-enhanced O₂ activation for efficient pollutant degradation.

carrier transfer (Fig. 7). First, Fe vacancies modulate the electronic structure, leading CB position to become more negative than $O_2/O_2^{\bullet-}$, which is a prerequisite for the reduction of O_2 to $O_2^{\bullet-}$ and the oxidation of $O_2^{\bullet-}$ to 1O_2 . Fe vacancies have induced significant electron delocalization and improved the conductivity of the material, which boosts carrier transport. In addition, Fe vacancies can act as electron trapping centers to prolong the carrier lifetime. Efficient carrier mobility and separation greatly increase the carrier's concentration on the surface and contribute to the generation of $O_2^{\bullet-}$ and 1O_2 by charge and energy transfer. Therefore, the abundant Fe vacancies on the surfaces of V_{Fe} -FeOCl optimally optimize the key process in photocatalytic O_2 activation, which greatly improves the yields of $O_2^{\bullet-}$ and 1O_2 and realizes the efficient photocatalytic degradation of pollutants.

4. Conclusion

We have synthesized a FeOCl photocatalyst rich in Fe vacancies (V_{Fe} -FeOCl) for efficient photocatalytic degradation of emerging pollutants via a facile method, and explored in detail the mechanism by which Fe vacancies enhance the catalytic effect. The concentration of the Fe vacancies was facilely controlled using a NaCl-assisted thermal decomposition approach. V_{Fe} -FeOCl exhibited superior performance compared to FeOCl, in terms of both reaction rate and mineralization rate, in the photocatalytic degradation of a variety of emerging pollutants, such as BPA. It is recyclable. It also showed great tolerance to a variety of environmental perturbations including coexisting inorganic ions and dissolved organic matter, pH change, and various water sources. The reactive oxygen species $O_2^{\bullet-}$ and 1O_2 are responsible for eliminating the pollutants, and their increased production on V_{Fe} -FeOCl leads to faster deterioration and more complete mineralization. We have analyzed in detail the mechanism of the enhanced photocatalytic performance of Fe vacancies by comprehensively characterizing their structure, electronic structure, photogenerated charge separation, and interfacial carrier transfer properties. It was found that Fe vacancies serve to modulate the electronic structure of V_{Fe} -FeOCl, resulting in a more negative CB potential. Furthermore, Fe vacancies enhance carriers separation and migration efficiency by acting as carrier trapping centers. This leads to V_{Fe} -FeOCl with higher carrier concentration, which greatly improves the reaction efficiency with O_2 and is more conducive to the efficient generation of ROS for pollutants degradation. Our results can be developed as a general method for the controlled synthesis of photocatalysts with cationic vacancies, as well as an inspiration for more effective utilization of O_2 and sunlight in the degradation of emerging pollutants.

CRediT authorship contribution statement

Zixuan Nie: Writing – original draft, Investigation, Data curation. **Chengji Sui:** Investigation. **Xiaobin Xie:** Investigation. **Shou-Qing Ni:** Funding acquisition. **Lingshuai Kong:** Investigation, Funding acquisition. **Yifeng Wang:** Investigation, Data curation. **Jinhua Zhan:** Project administration, Investigation, Funding acquisition.

Declaration of Competing Interest

The authors declare that they have no known competing financial interests or personal relationships that could have appeared to influence the work reported in this paper.

Data Availability

Data will be made available on request.

Acknowledgements

This work was supported by the Key Research & Developmental Program of Shandong Province (2021CXGC011202), National Natural

Science Foundation of China (Grant Nos. 22276110, 22106088) and Fundamental Research Funds of Shandong University (zy202102).

Appendix A. Supporting information

Supplementary data associated with this article can be found in the online version at doi:10.1016/j.apcatb.2024.123819.

References

- [1] K.H. Cochran, D.C. Westerman, C.C. Montagner, S. Coffin, L. Diaz, B. Fryer, G. Harraka, E.G. Xu, Y. Huang, D. Schlenk, D.D. Dionysiou, S.D. Richardson, Chlorination of emerging contaminants for application in potable wastewater reuse: disinfection byproduct formation, estrogen activity, and cytotoxicity, Environ. Sci. Technol. 58 (2024) 704–716, <https://doi.org/10.1021/acs.est.3c05978>.
- [2] S. Wang, Y. Lin, B. Shao, H. Dong, J. Ma, X. Guan, Selective removal of emerging organic contaminants from water using electrogenerated Fe(IV) and Fe(V) under near-neutral conditions, Environ. Sci. Technol. 57 (2023) 9332–9341, <https://doi.org/10.1016/j.est.3c01850>.
- [3] Y. Yu, D. Tong, Y. Yu, D. Tian, W. Zhou, X. Zhang, W. Shi, G. Liu, Toxic effects of four emerging pollutants on cardiac performance and associated physiological parameters of the thick-shell mussel (*Mytilus coruscus*), Environ. Pollut. 334 (2023) 122244, <https://doi.org/10.1016/j.envpol.2023.122244>.
- [4] J. Xu, Y. Yao, C. Zhu, L. Lu, Q. Fang, Z. He, S. Song, B. Chen, Y. Shen, Unveiling enhanced electron-mediated peroxymonosulfate activation for degradation of emerging organic pollutants, Appl. Catal. B-Environ. 341 (2024) 123356, <https://doi.org/10.1016/j.apcatb.2023.123356>.
- [5] J.-Q. Chen, G.-N. Zhou, R.-R. Ding, Q. Li, H.-Q. Zhao, Y. Mu, Ferrous ion enhanced Fenton-like degradation of emerging contaminants by sulfidated nanosized zero-valent iron with pH insensitivity, J. Hazard. Mater. 459 (2023) 132229, <https://doi.org/10.1016/j.jhazmat.2023.132229>.
- [6] Z.-Y. Dong, Y.-L. Lin, T.-Y. Zhang, C.-Y. Hu, Y. Pan, Z.-X. Zheng, Y.-L. Tang, B. Xu, N.-Y. Gao, Enhanced degradation of emerging contaminants by permanganate/quinone process: case study with bisphenol A, Water Res 219 (2022) 118528, <https://doi.org/10.1016/j.watres.2022.118528>.
- [7] P.D. Jepson, R.J. Law, Persistent pollutants, persistent threats, Science 352 (2016) 1388–1389, <https://doi.org/10.1126/science.aaf9075>.
- [8] S. Moradi, A.A. Isari, F. Hayati, R. Rezaei Kalantary, B. Kakavandi, Co-implanting of TiO_2 and liquid-phase-delaminated $g-C_3N_4$ on multi-functional graphene nanobridges for enhancing photocatalytic degradation of acetaminophen, Chem. Eng. J. 414 (2021) 128618, <https://doi.org/10.1016/j.cej.2021.128618>.
- [9] D. Zhang, Y. Li, P. Wang, J. Qu, S. Zhan, Y. Li, Regulating spin polarization through cationic vacancy defects in $Bi_4Ti_3O_{12}$ for enhanced molecular oxygen activation, Angew. Chem. Int. Ed. 62 (2023) e202303807, <https://doi.org/10.1002/anie.202303807>.
- [10] H. Xu, X. Liu, H. Li, L. Zhang, O_2 activation and 1O_2 generation over phosphate modified BiOCl for efficient photodegradation of organic pollutants, Appl. Catal. B-Environ. 314 (2022) 121520, <https://doi.org/10.1016/j.apcatb.2022.121520>.
- [11] Z. Zhou, Z. Shen, C. Song, M. Li, H. Li, S. Zhan, Boosting the activation of molecular oxygen and the degradation of tetracycline over high loading Ag single atomic catalyst, Water Res 201 (2021) 117314, <https://doi.org/10.1016/j.watres.2021.117314>.
- [12] V.-H. Nguyen, M. Mousavi, J.B. Ghasemi, Q.V. Le, S.A. Delbari, M. Shahedi Asl, M. Shokouhimehr, M. Mohammadi, Y. Azizian-Kalandaragh, A. Sabahi Namini, In situ preparation of $g-C_3N_4$ nanosheet/FeOCl: achievement and promoted photocatalytic nitrogen fixation activity, J. Colloid Interf. Sci. 587 (2021) 538–549, <https://doi.org/10.1016/j.jcis.2020.11.011>.
- [13] S. Vadivel, M. Fujii, S. Rajendran, Facile synthesis of broom stick like FeOCl- $g-C_3N_5$ nanocomposite as novel Z-scheme photocatalysts for rapid degradation of pollutants, Chemosphere 307 (2022) 135716, <https://doi.org/10.1016/j.chemosphere.2022.135716>.
- [14] J. Zhang, G. Zhang, Q. Ji, H. Lan, J. Qu, H. Liu, Carbon nanodot-modified FeOCl for photo-assisted Fenton reaction featuring synergistic in-situ H_2O_2 production and activation, Appl. Catal. B-Environ. 266 (2020) 118665, <https://doi.org/10.1016/j.apcatb.2020.118665>.
- [15] X. Zhang, X. Li, P. Yu, Y. Yu, X. Fan, J. Zhang, Y. Yu, H. Zheng, Y. Sun, Photocatalytic O_2 activation by metal-free carbon nitride nanotube for rapid reactive species generation and organic contaminants degradation, J. Hazard. Mater. 456 (2023) 131715, <https://doi.org/10.1016/j.jhazmat.2023.131715>.
- [16] M. Sabri, A. Habibi-Yangieh, H. Chand, V. Krishnan, Activation of persulfate by novel TiO_2 /FeOCl photocatalyst under visible light: Facile synthesis and high photocatalytic performance, Sep. Purif. Technol. 250 (2020) 117268, <https://doi.org/10.1016/j.seppur.2020.117268>.
- [17] D.-L. Bao, A. O'Hara, S. Du, S.T. Pantelides, Tunable, ferroelectricity-inducing, spin-spiral magnetic ordering in monolayer FeOCl, Nano Lett. 22 (2022) 3598–3603, <https://doi.org/10.1021/acs.nanolett.1c05043>.
- [18] Y. Nosaka, A.Y. Nosaka, Generation and detection of reactive oxygen species in photocatalysis, Chem. Rev. 117 (2017) 11302–11336, <https://doi.org/10.1021/acs.chemrev.7b00161>.
- [19] S. Jiang, H. Zheng, X. Sun, M. Zhu, Y. Zhou, D. Wang, D. Zhang, L. Zhang, New and highly efficient Ultra-thin $g-C_3N_4$ /FeOCl nanocomposites as photo-Fenton catalysts for pollutants degradation and antibacterial effect under visible light,

Chemosphere 290 (2022) 133324, <https://doi.org/10.1016/j.chemosphere.2021.133324>.

[20] J. Song, M. Zhang, C. Yan, X. Zhao, G. Liu, J. Zhang, AgSCN/AgCl/FeOCl nanosheets heterojunction with novel interface structure and excellent photocatalytic performance, *J. Alloy. Compd.* 836 (2020) 155544, <https://doi.org/10.1016/j.jallcom.2020.155544>.

[21] H. Guo, Y. Deng, H. Yin, J. Liu, S. Zou, Fabricating BiOCl nanoflake/FeOCl nanospindle heterostructures for efficient visible-light photocatalysis, *Molecules* (2023).

[22] S. Asadzadeh-Khaneghah, A. Habibi-Yangjeh, D. Seifzadeh, H. Chand, V. Krishnan, Visible-light-activated g-C₃N₄ nanosheet/carbon dot/FeOCl nanocomposites: photodegradation of dye pollutants and tetracycline hydrochloride, *Colloids Surf. A* 617 (2021) 126424, <https://doi.org/10.1016/j.colsurfa.2021.126424>.

[23] X. Jiao, Z. Chen, X. Li, Y. Sun, S. Gao, W. Yan, C. Wang, Q. Zhang, Y. Lin, Y. Luo, Y. Xie, Defect-mediated electron-hole separation in one-unit-cell ZnIn₂S₄ layers for boosted solar-driven CO₂ reduction, *J. Am. Chem. Soc.* 139 (2017) 7586–7594, <https://doi.org/10.1021/jacs.7b02290>.

[24] J. Wang, W. Jiang, D. Liu, Z. Wei, Y. Zhu, Photocatalytic performance enhanced via surface bismuth vacancy of Bi₄S₂O₁₅ core/shell nanowires, *Appl. Catal. B-Environ.* 176–177 (2015) 306–314, <https://doi.org/10.1016/j.apcatb.2015.04.022>.

[25] L. Zhang, Z. Wang, C. Hu, B. Shi, Enhanced photocatalytic performance by the synergy of Bi vacancies and Bi⁰ in Bi₂-δMoO₆, *Appl. Catal. B-Environ.* 257 (2019) 117785, <https://doi.org/10.1016/j.apcatb.2019.117785>.

[26] Z. Zhao, G. Ren, Z. Zhang, X. Meng, Z. Li, Rapid Joule heating synthesis of Pt clusters on C₃N₄ with abundant nitrogen vacancies for highly-efficiently photocatalytic H₂ production, *Sep. Purif. Technol.* 330 (2024) 125393, <https://doi.org/10.1016/j.seppur.2023.125393>.

[27] S. Wang, L. Pan, J.-J. Song, W. Mi, J.-J. Zou, L. Wang, X. Zhang, Titanium-defected undoped anatase TiO₂ with p-type conductivity, room-temperature ferromagnetism, and remarkable photocatalytic performance, *J. Am. Chem. Soc.* 137 (2015) 2975–2983, <https://doi.org/10.1021/ja512047k>.

[28] Q. Li, F.-t Li, Recent advances in molecular oxygen activation via photocatalysis and its application in oxidation reactions, *Chem. Eng. J.* 421 (2021) 129915, <https://doi.org/10.1016/j.cej.2021.129915>.

[29] Y. Liu, C. Xiao, Z. Li, Y. Xie, Vacancy engineering for tuning electron and phonon structures of two-dimensional materials, *Adv. Energy Mater.* 6 (2016) 1600436, <https://doi.org/10.1002/aenm.201600436>.

[30] W. Ding, S. Yuan, Y. Yang, X. Li, M. Luo, Defect engineering: the role of cationic vacancies in photocatalysis and electrocatalysis, *J. Mater. Chem. A* 11 (2023) 23653–23682, <https://doi.org/10.1039/D3TA04947G>.

[31] P.J. Panteix, I. Julien, P. Abéard, D. Bernache-Assollant, Influence of cationic vacancies on the ionic conductivity of oxyapatites, *J. Eur. Ceram. Soc.* 28 (2008) 821–828, <https://doi.org/10.1016/j.jeurceramsoc.2007.07.019>.

[32] S. Liu, X. Mu, W. Li, M. Lv, B. Chen, C. Chen, S. Mu, Cation vacancy-modulated PtPdRuTe five-fold twinned nanomaterial for catalyzing hydrogen evolution reaction, *Nano Energy* 61 (2019) 346–351, <https://doi.org/10.1016/j.nanoen.2019.04.086>.

[33] C. Tan, Q. Xu, T. Sheng, X. Cui, Z. Wu, H. Gao, H. Li, Reactive oxygen species generation in FeOCl nanosheets activated peroxymonosulfate system: radicals and non-radical pathways, *J. Hazard. Mater.* 398 (2020) 123084, <https://doi.org/10.1016/j.jhazmat.2020.123084>.

[34] G. Kresse, J. Furthmüller, Efficiency of ab-initio total energy calculations for metals and semiconductors using a plane-wave basis set, *Comp. Mater. Sci.* 6 (1996) 15–50, [https://doi.org/10.1016/0927-0256\(96\)00008-0](https://doi.org/10.1016/0927-0256(96)00008-0).

[35] J.P. Perdew, K. Burke, M. Ernzerhof, Generalized gradient approximation made simple, *Phys. Rev. Lett.* 77 (1996) 3865–3868, <https://doi.org/10.1103/PhysRevLett.77.3865>.

[36] S. Grimme, J. Antony, S. Ehrlich, H. Krieg, A consistent and accurate ab initio parametrization of density functional dispersion correction (DFT-D) for the 94 elements H–Pu, *J. Chem. Phys.* 132 (2010), <https://doi.org/10.1063/1.3382344>.

[37] M. Sun, C. Chu, F. Geng, X. Lu, J. Qu, J. Crittenden, M. Elimelech, J.-H. Kim, Reinventing Fenton chemistry: iron oxychloride nanosheet for pH-Insensitive H₂O₂ activation, *Environ. Sci. Technol. Lett.* 5 (2018) 186–191, <https://doi.org/10.1021/acs.estlett.8b00065>.

[38] J. Wang, X. Liu, T. Liao, C. Ma, B. Chen, Y. Li, X. Fan, W. Peng, Fe doping induced selenium vacancy on cobalt selenide for enhanced hydrogen peroxides production, *Appl. Catal. B-Environ.* 341 (2024) 123344, <https://doi.org/10.1016/j.apcatb.2023.123344>.

[39] X. Hao, Y. Wang, J. Zhou, Z. Cui, Y. Wang, Z. Zou, Zinc vacancy-promoted photocatalytic activity and photostability of ZnS for efficient visible-light-driven hydrogen evolution, *Appl. Catal. B-Environ.* 221 (2018) 302–311, <https://doi.org/10.1016/j.apcatb.2017.09.006>.

[40] J. Wang, K.-P. Hou, Y. Wen, H. Liu, H. Wang, K. Chakarawet, M. Gong, X. Yang, Interlayer structure manipulation of iron oxychloride by potassium cation intercalation to steer H₂O₂ activation pathway, *J. Am. Chem. Soc.* 144 (2022) 4294–4299, <https://doi.org/10.1021/jacs.1c12398>.

[41] A.E. ElMetwally, G. Eshaq, F.Z. Yehia, A.M. Al-Sabagh, S. Kegnæs, Iron oxychloride as an efficient catalyst for selective hydroxylation of benzene to phenol, *ACS Catal.* 8 (2018) 10668–10675, <https://doi.org/10.1021/acscatal.8b03590>.

[42] X. Liu, L. Zhao, H. Xu, Q. Huang, Y. Wang, C. Hou, Y. Hou, J. Wang, F. Dang, J. Zhang, Tunable cationic vacancies of cobalt oxides for efficient electrocatalysis in Li-O₂ batteries, *Adv. Energy Mater.* 10 (2020) 2001415, <https://doi.org/10.1002/aenm.202001415>.

[43] J. Luo, M. Sun, C.L. Ritt, X. Liu, Y. Pei, J.C. Crittenden, M. Elimelech, Tuning Pb(II) adsorption from aqueous solutions on ultrathin iron oxychloride (FeOCl) nanosheets, *Environ. Sci. Technol.* 53 (2019) 2075–2085, <https://doi.org/10.1021/acs.est.8b07027>.

[44] Y. Kang, Z. Mao, Y. Wang, C. Pan, M. Ou, H. Zhang, W. Zeng, X. Ji, Design of a two-dimensional interplanar heterojunction for catalytic cancer therapy, *Nat. Commun.* 13 (2022) 2425, <https://doi.org/10.1038/s41467-022-30166-1>.

[45] Y. Yu, W. Yan, X. Wang, P. Li, W. Gao, H. Zou, S. Wu, K. Ding, Surface engineering for extremely enhanced charge separation and photocatalytic hydrogen evolution on g-C₃N₄, *Adv. Mater.* 30 (2018) 1705060, <https://doi.org/10.1002/adma.201705060>.

[46] D. Ji, S. Wang, X. Ge, X. Xiao, L. Wang, Z. Zeng, C. Zhang, Effect of calcination temperature on B-site vacancy content of La_{0.75}Sr_{0.25}Mn_{0.92}Δ_{0.08}O_{3-δ} perovskite, *J. Rare Earth* 36 (2018) 287–297, <https://doi.org/10.1016/j.jre.2017.05.014>.

[47] S.O.J. Long, A.V. Powell, P. Vaqueiro, S. Hull, High thermoelectric performance of bornite through control of the Cu(II) content and vacancy concentration, *Chem. Mater.* 30 (2018) 456–464, <https://doi.org/10.1021/acs.chemmater.7b04436>.

[48] R. Zhang, L. Pan, B. Guo, Z.-F. Huang, Z. Chen, L. Wang, X. Zhang, Z. Guo, W. Xu, K.P. Loh, J.-J. Zou, Tracking the role of defect types in Co₃O₄ structural evolution and active motifs during oxygen evolution reaction, *J. Am. Chem. Soc.* 145 (2023) 2271–2281, <https://doi.org/10.1021/jacs.2c10515>.

[49] M. Li, J. Sun, X. Zhou, H. Yao, B. Cong, Y. Li, G. Chen, Modulating negative magnetoresistance via inducing vacancy for regulates electron transport under magnetic ambient conditions, *Appl. Catal. B-Environ.* 322 (2023) 122096, <https://doi.org/10.1016/j.apcatb.2022.122096>.

[50] L. Wang, R. Wang, T. Qiu, L. Yang, Q. Han, Q. Shen, X. Zhou, Y. Zhou, Z. Zou, Bismuth vacancy-induced efficient CO₂ photoreduction in BiOCl directly from natural air: a progressive step toward photosynthesis in nature, *Nano Lett.* 21 (2021) 10260–10266, <https://doi.org/10.1021/acs.nanolett.1c03249>.

[51] L. Peng, N. Yang, Y. Yang, Q. Wang, X. Xie, D. Sun-Waterhouse, L. Shang, T. Zhang, G.I.N. Waterhouse, Atomic cation-vacancy engineering of NiFe-layered double hydroxides for improved activity and stability towards the oxygen evolution reaction, *Angew. Chem. Int. Ed.* 60 (2021) 24612–24619, <https://doi.org/10.1002/anie.202109938>.

[52] B. Liu, Y. Wang, H.-Q. Peng, R. Yang, Z. Jiang, X. Zhou, C.-S. Lee, H. Zhao, W. Zhang, Iron vacancies induced bifunctionality in ultrathin feroxyhyte nanosheets for overall water splitting, *Adv. Mater.* 30 (2018) 1803144, <https://doi.org/10.1002/adma.201803144>.

[53] W.-D. Oh, L.-W. Lok, A. Veksha, A. Giannis, T.-T. Lim, Enhanced photocatalytic degradation of bisphenol A with Ag-decorated S-doped g-C₃N₄ under solar irradiation: Performance and mechanistic studies, *Chem. Eng. J.* 333 (2018) 739–749, <https://doi.org/10.1016/j.cej.2017.09.182>.

[54] L. Kong, G. Fang, X. Xi, Y. Wen, Y. Chen, M. Xie, F. Zhu, D. Zhou, J. Zhan, A novel peroxymonosulfate activation process by periclaste for efficient singlet oxygen-mediated degradation of organic pollutants, *Chem. Eng. J.* 403 (2021) 126445, <https://doi.org/10.1016/j.cej.2020.126445>.

[55] Y. Ding, P. Zhou, H. Tang, Visible-light photocatalytic degradation of bisphenol A on NaBiO₃ nanosheets in a wide pH range: a synergistic effect between photocatalytic oxidation and chemical oxidation, *Chem. Eng. J.* 291 (2016) 149–160, <https://doi.org/10.1016/j.cej.2016.01.105>.

[56] F. Yang, F. Zhao, Mechanism of visible light enhances microbial degradation of Bisphenol A, *J. Hazard. Mater.* 443 (2023) 130214, <https://doi.org/10.1016/j.jhazmat.2022.130214>.

[57] H. Zhan, Q. Zhou, M. Li, R. Zhou, Y. Mao, P. Wang, Photocatalytic O₂ activation and reactive oxygen species evolution by surface B-N bond for organic pollutants degradation, *Appl. Catal. B-Environ.* 310 (2022) 121329, <https://doi.org/10.1016/j.apcatb.2022.121329>.

[58] J. Hu, F. Chen, K. Mu, J. Zhang, J. Lu, Enhanced photocatalytic O₂ activation by the synergy of efficient oxygen adsorption and interfacial charge separation: a case of Bi₃O₄Br/rGO van der Waals heterojunction, *Sep. Purif. Technol.* 286 (2022) 120416, <https://doi.org/10.1016/j.seppur.2021.120416>.

[59] R. Luo, M. Li, C. Wang, M. Zhang, M.A. Nasir Khan, X. Sun, J. Shen, W. Han, L. Wang, J. Li, Singlet oxygen-dominated non-radical oxidation process for efficient degradation of bisphenol A under high salinity condition, *Water Res* 148 (2019) 416–424, <https://doi.org/10.1016/j.watres.2018.10.087>.

[60] Z. Kang, E. Lin, N. Qin, J. Wu, D. Bao, Bismuth vacancy-mediated quantum dot precipitation to trigger efficient piezocatalytic activity of Bi₂WO₆ nanosheets, *ACS Appl. Mater. Inter.* 14 (2022) 11375–11387, <https://doi.org/10.1021/acsami.1c23282>.

[61] X. Dai, Z. Han, G.I.N. Waterhouse, H. Fan, S. Ai, Ordered graphitic carbon nitride tubular bundles with efficient electron-hole separation and enhanced photocatalytic performance for hydrogen generation, *Appl. Catal. A: Gen.* 566 (2018) 200–206, <https://doi.org/10.1016/j.apcata.2018.09.001>.

[62] J. Di, C. Chen, C. Zhu, P. Song, J. Xiong, M. Ji, J. Zhou, Q. Fu, M. Xu, W. Hao, J. Xia, S. Li, H. Li, Z. Liu, Bismuth vacancy-tuned bismuth oxybromide ultrathin nanosheets toward photocatalytic CO₂ reduction, *ACS Appl. Mater. Inter.* 11 (2019) 30786–30792, <https://doi.org/10.1021/acsami.9b08109>.

[63] W. Yang, Y. Zhu, F. You, L. Yan, Y. Ma, C. Lu, P. Gao, Q. Hao, W. Li, Insights into the surface-defect dependence of molecular oxygen activation over birnessite-type MnO₂, *Appl. Catal. B-Environ.* 233 (2018) 184–193, <https://doi.org/10.1016/j.apcatb.2018.03.107>.

[64] R. Zhang, Y.-C. Zhang, L. Pan, G.-Q. Shen, N. Mahmood, Y.-H. Ma, Y. Shi, W. Jia, L. Wang, X. Zhang, W. Xu, J.-J. Zou, Engineering cobalt defects in cobalt oxide for highly efficient electrocatalytic oxygen evolution, *ACS Catal.* 8 (2018) 3803–3811, <https://doi.org/10.1021/acscatal.8b01046>.